Supporting Information

Impact of bimetallic synergies on Mo-doping NiFeOOH: Insights into enhanced OER activity and reconstructed electronic structure

Jingkuo Qu, Yuchen Dong, Tuo Zhang, Chang Zhao, Liting Wei, Xiangjiu Guan (✉)

International Research Center for Renewable Energy, State Key Laboratory of Multiphase Flow in Power Engineering, Xi'an Jiaotong University, Xi'an 710049, China

Received Apr. 25, 2024; accepted Jul. 13, 2024;

Correspondence: Xiangjiu Guan, xj-guan@mail.xjtu.edu.cn

Characterizations

X-ray diffraction(XRD) patterns were collected utilizing a PANalytical X'pert MPD Pro diffractometer with Cu Kα radiation ($\lambda = 0.15406$ Å). The 2θ covered in the data collection ranged from 30° to 80° and obtained in the Bragg-Brentano mode at a scan rate of 5° min^{-1}. X-ray photoelectron spectroscopy measurements were conducted on a Kratos spectrometer (AXIS Ultra DLD) with Al Kα radiation. The calibration for binding energy (BE) was established with reference to the C 1s peak at 284.8 eV. Scanning electron microscopy (SEM) was conducted using a JEOL JSM-7800F instrument, which was operated at an acceleration voltage of 15 kV. Transmission electron microscopy (TEM) images were captured using an FEI Tecnai G2 F30 S-TWIN instrument at an acceleration voltage of 300 kV. Selected-area electron diffraction (SAED) and energy-dispersive X-ray spectroscopy mapping (EDS) were executed with an OX-FORD MAX-80 detector equipped with a STEM aberration corrector, functioning at 200 kV. Raman scattering analysis was performed with an argon ion laser (532 nm, 20 mW, Jobin Yvon LabRAM HR800) in a diluted 0.1 M KOH electrolyte. The purpose of this was to safeguard the Raman detector lens from corrosion, as it was immersed in the KOH electrolyte during operando spectroscopic examinations. The use of a low KOH electrolyte concentration helped alleviate the disruptive influence of gas bubbles during water oxidation.

Electrochemical measurement

Electrochemical analysis was conducted using a three-electrode system with a CHI-760D electrochemical workstation. A 1.0 M KOH aqueous solution served as the electrolyte, with the catalyst prepared at 1 cm × 1 cm, a platinum plate at 2 cm × 2 cm, and a Hg/HgO electrode in 1.0 M KOH (CHI 152) used as the working electrode (WE), counter electrode (CE), and reference electrode (RE), respectively. All electrode potentials were referenced against the reversible hydrogen electrode (versus RHE) and the tests were performed at room temperature (27 °C). Prior to activating the WE, cyclic voltammetry (CV) plots were obtained with a scan rate of 100 mV/s for at least 40

cycles. Polarization curves were then generated at 5 mV/s with 95% iR correction, taking into account the ohmic loss of the solution. To convert the measured potentials into the reversible hydrogen electrode (RHE) scale, the Nernst equation was utilized.

$$E(\text{versus RHE})=E(\text{versus Hg/HgO})+0.098+0.059\times\text{pH} \quad (1)$$

where E(versus RHE) and E(versus Hg/HgO) represent the voltage relative to the reversible hydrogen electrode and Hg/HgO reference electrode, respectively.

Tafel slope was determined from the polarization curves using a specific equation

$$\eta=b\times\log(|j|)+\text{a} \quad (2)$$

where η, j, b, and a represent the overpotential, current density, tafel slope, and a constant, respectively.

For the stability testing of MoNiFe/NF electrodes, the chronoamperometry method was employed. The electrochemical surface area (ECSA) was estimated by measuring the double-layer capacitance (C_{dl}) of the electrodes, including MoNiFe/NF, NiFe/NF, NiMo/NF, and Ni/NF. This measurement was obtained through cyclic voltammetry at various scan rates to indicate the number of active sites on the surface. Additionally, electrochemical impedance spectroscopy (EIS) was performed at 1.5 V versus RHE across a frequency range from 100 kHz to 10 MHz with an amplitude of 10 mV.

The turnover frequency (TOF) value demonstrates the rate at which oxygen is generated over time and was determined using electrochemical measurements. Active site loading was determined by performing continuous CV scans at various rates (2.5 to 15 mV/s) in a 1.0 M KOH solution at a potential of 0.25–0.6 V versus Hg/HgO. By analyzing the oxidative current response in relation to the scan rate through linear regression, Eq. (3) was derived to calculate the number of active sites.

$$\text{Slope}=n^2F^2A\Gamma/4\text{R}T \quad (3)$$

where n represents the electrons transferred during oxidation (n = 1), F is the Faradic constant (96485.3 C/mol), A is the area of the electrode (1 cm^2), Γ is the active site density ($mol\cdot cm^{-2}$), while R and T correspond to the universal gas constant and absolute temperature. The moles of active sites participating in the OER can be calculated by multiplying A by Γ.

$$m=A\times\Gamma \quad (4)$$

Subsequently, the TOF values were computed to evaluate the activity of the

MoNiFe/NF catalyst. This calculation was conduceted using

$$TOF = jS/4Fm \quad (5)$$

where j denotes the current density (mA cm^{-2}) measured at φ = 0.27 V, S is the surface area of NF (1 cm^2), and 4 signifies the four-electron transfer during the OER catalytic process. F stands for the Faraday constant, and m is the moles of active sites within the samples, calculated based on the loading on the WE.

Theoretical calculations

In this study, spin-polarized density functional theory (DFT) calculations were performed using the state-of-the-art Vienna ab initio simulation package (VASP) [1–3] to elucidate the underlying mechanism behind the remarkable electrocatalytic activity of MoNiFe/NF for the OER. The exchange-correlation interactions were described by the Perdue-Burke-Ernzerhof (PBE) version of the generalized gradient approximation (GGA) [4]. The core-valence electron interactions were modeled using the highly accurate projector-augmented wave (PAW) method [5,6]. A stringent energy convergence threshold of 1 meV/atom was adopted to ensure high precision, with an energy cutoff of up to 450 eV. The partial occupancies of orbitals were determined using the Gaussian smearing method with a narrow smearing width of 0.05 eV. To account for the van der Waals interactions, the DFT-D3 correction was applied. The Brillouin zone was sampled with a 3 × 3 × 1 Gamma-centered grid. The energy and force convergence criteria were set to a remarkable level of 10^{-6} eV and 0.02 eV/Å, respectively. Moreover, the calculations incorporated Hubbard-U terms for Ni and Fe with effective U values of 5.5 and 4.30 eV, respectively, to accurately describe their electron correlations [7].

The slab models of NiFe/NF used in the LOM pathway[8] were terminated by the (001) surface containing two layers of metal (oxy)hydroxides as shown in Fig. S11, to eliminate the interaction between periodic slabs, the thickness of vacuum spaces was 15 Å. The mole ratio of Ni and Fe in the original NiFe/NF bulk model was 3 : 1. To determine the stable configuration of Mo doping, several slab models featuring different

Mo sites were constructed as shown in Fig. S12. The relative stability of Mo replacement was evaluated via the computation of the formation energy (ΔE_f), expressed as

$$\Delta E_f = E_{slab} - \sum N_i E_i \quad (6)$$

where E_{slab}, E_i, and N_i denote the total energies of the slab model, the energy, and the number of the ith element, respectively. The calculations reveal that the Mo atom exhibits a preference for replacing the Ni4 site, with the most negative ΔE_f value observed for this site as shown in Fig. S13.

Determining the lower Hubbard band and upper Hubbard band centers

The lower Hubbard band (LHB) was determined by the 3d-orbital distribution below E_F in the density of states (DOS) diagrams, while the upper Hubbard band(UHB) was determined by the unoccupied 3d-orbitals distribution above E_F. The center of LHB and UHB were calculated by

$$\bar{\varepsilon}\mathrm{LHB} = \frac{\int_{-\infty}^{0} n(\varepsilon)\varepsilon d\varepsilon}{\int_{-\infty}^{0} n(\varepsilon) d\varepsilon} \quad (7)$$

and

$$\bar{\varepsilon}\mathrm{LHB} = \frac{\int_{0}^{+\infty} n(\varepsilon)\varepsilon d\varepsilon}{\int_{0}^{+\infty} n(\varepsilon) d\varepsilon} \quad (8)$$

where ε and $n(\varepsilon)$ are the energy level and number of states at this energy level, respectively.

Oxygen vacancy formation energy calculation

The formation energy of oxygen vacancy (ΔG_{Ov}) was calculated with respect to the Gibbs free energy of O_2 at 298.15 K and 1.0 bar.

$$\Delta G_{ov} = \frac{1}{2} G_{O_2} + G_{ov} - G_{surface} \quad (9)$$

where G_{O2}, G_{Ov}, and $G_{surface}$ are Gibbs free energies of O_2, surface with oxygen vacancy, and the clean surface, respectively. Since DFT calculations are inaccurate at describing the oxygen molecules, the Gibbs free energy of O_2 was calculated by

$$G_{O_2} = 2G_{H_2O} + 2G_{H_2} + 4.92 \text{ eV} \quad (10)$$

where G_{H_2O} and G_{H_2} are Gibbs free energies of H_2O and H_2, respectively. The Gibbs free energy change of $H_2O \rightarrow H_2+O_2$ is 4.92 eV.

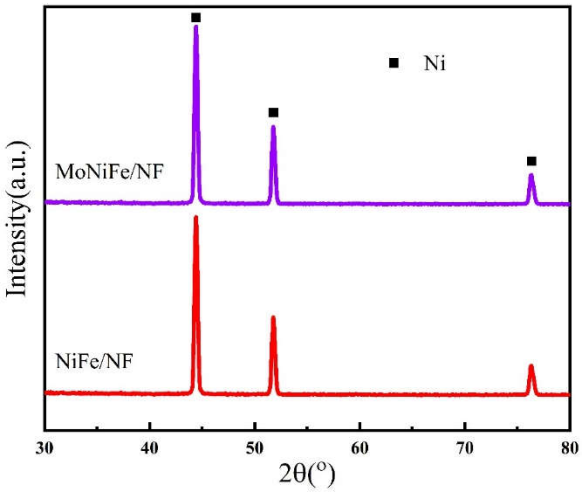

Fig. S1 XRD patterns MoNiFe/NF and NiFe/NF.

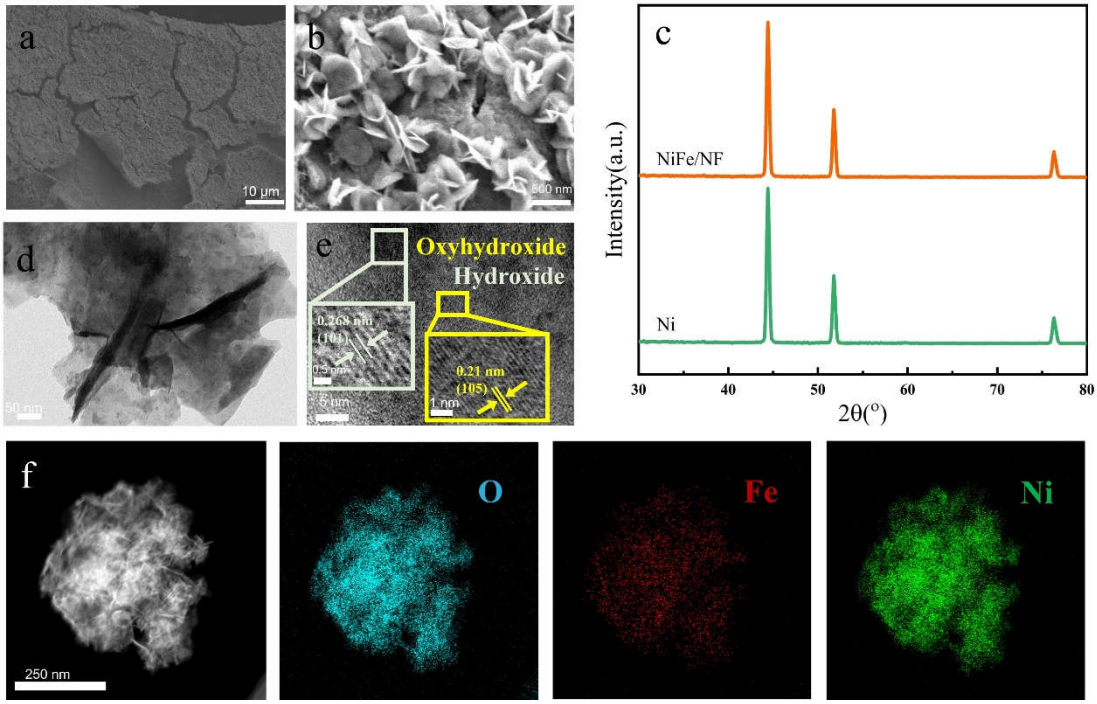

Fig. S2 Preparation and characterizations of NiFe/NF.

(a, b) SEM images; (c)XRD patterns of NiFe/NF; (d) high-resolution transmission electron microscopy (HRTEM) images withlow magnification; (e) high magnification; (f) EDS mapping images.

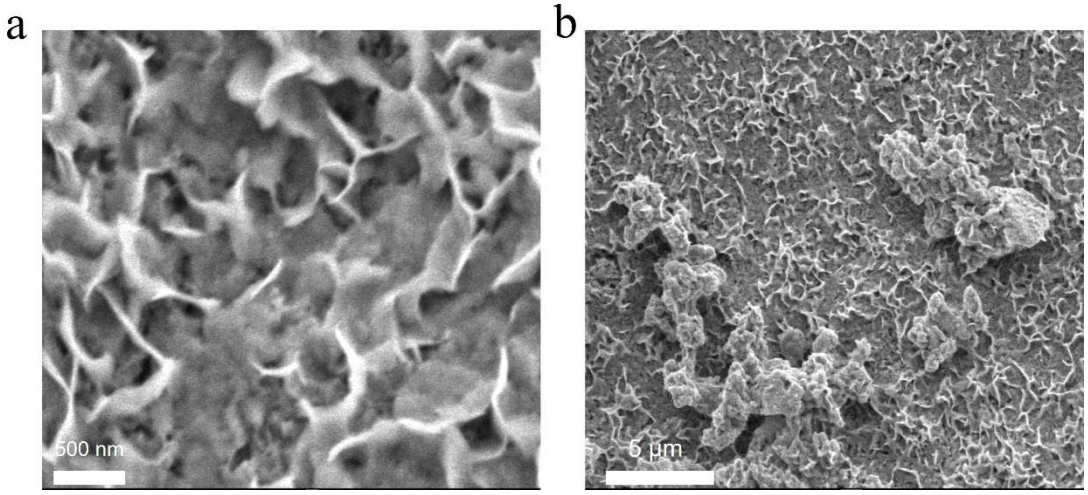

Fig. S3 SEM images of MoNiFe/NF with different magnifications.

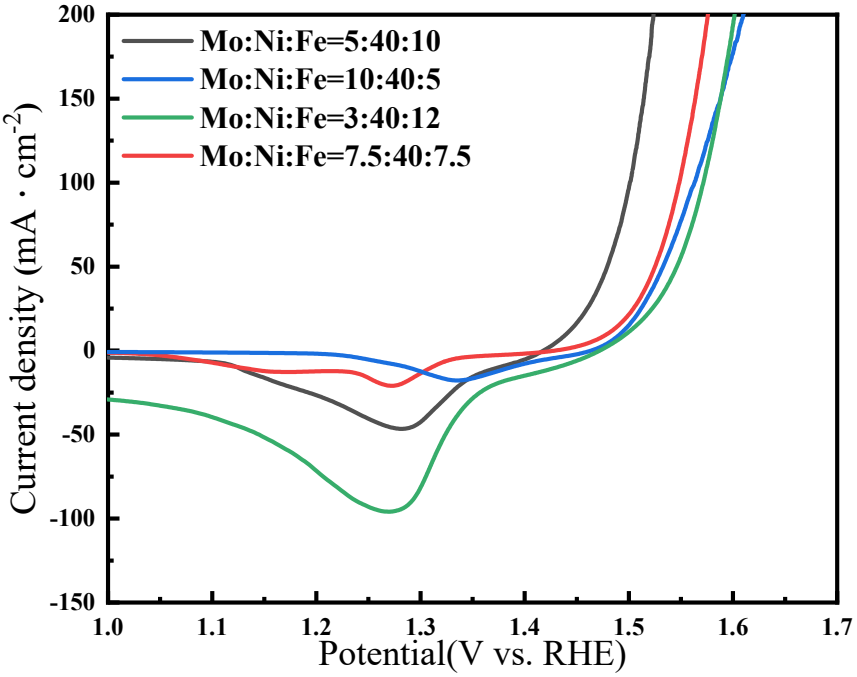

Fig. S4 Polarization curves of MoNiFe/NF catalysts at different raw material feed ratios (At a ratio of 1 : 8 : 2 (5 : 40: 10), MoNiFe/NF shows the best performance).

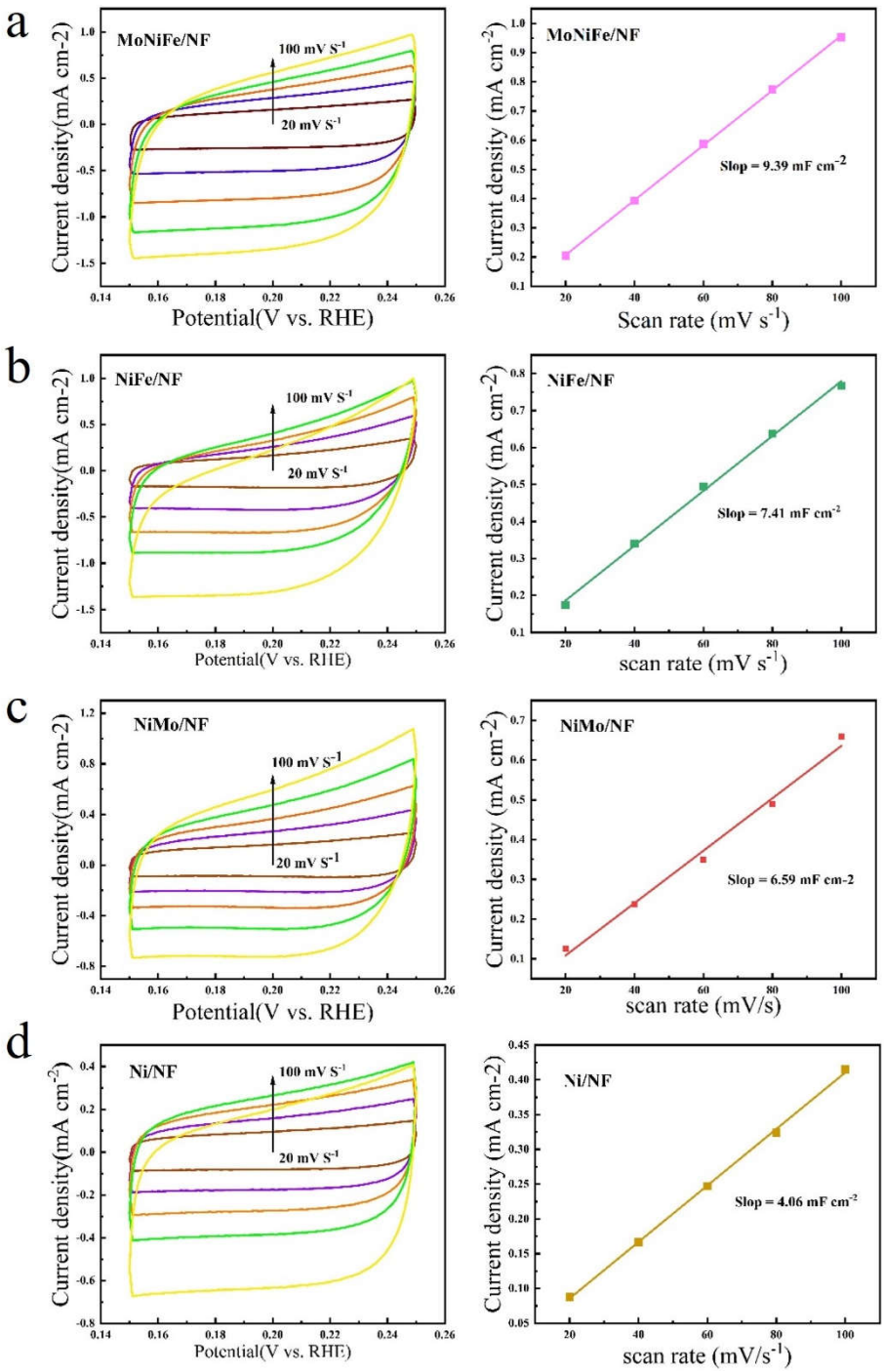

Fig. S5 CV curves of catalytic electrodes at various scan rates to investigate the specific C_{dl} that was used to estimate the electrochemical active specific surface area for OER.

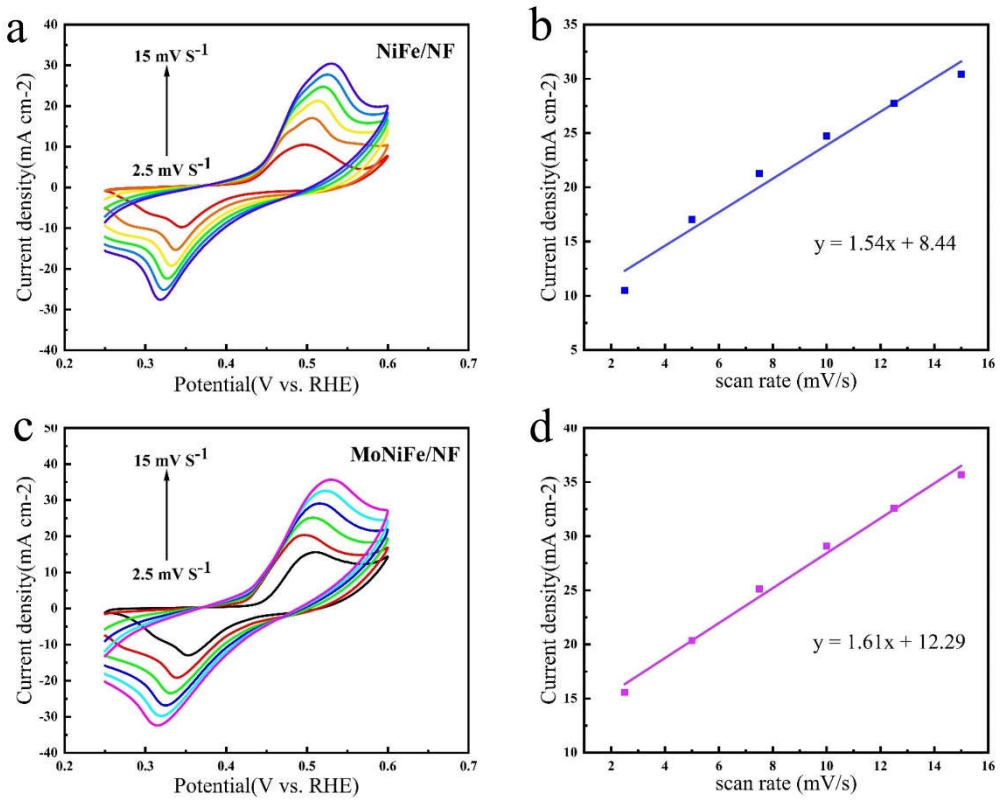

Fig. S6 CV scans and the anodic charging currents as a function of scan rate.
(a) CV test for NiFe/NF; (b) anodic charging currents as a function of scan rate for NiFe/NF; (c) CV test for MoNiFe/NF; (d) anodic charging currents as a function of scan rate for MoNiFe/NF.

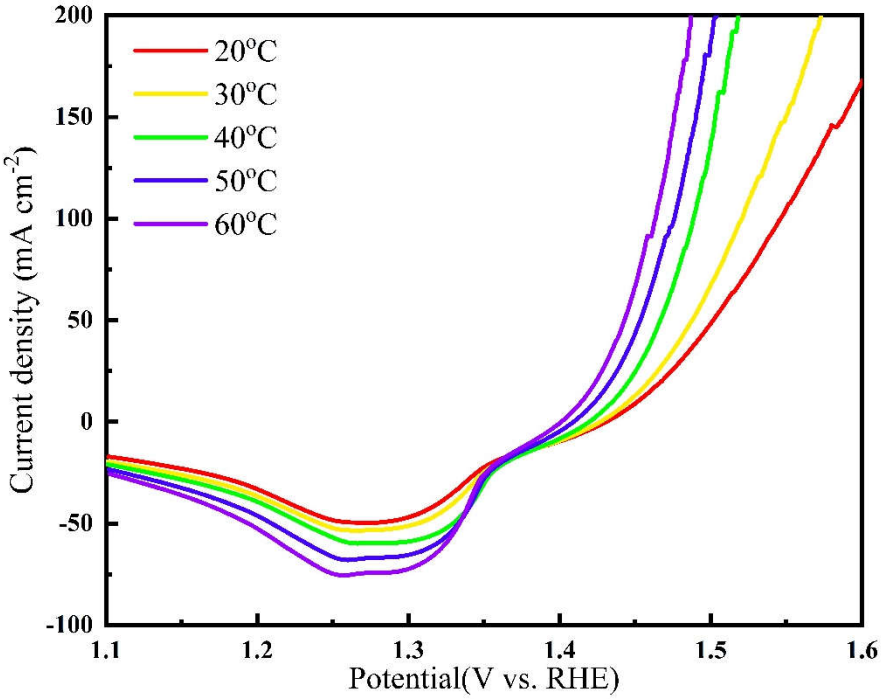

Fig. S7 Temperature-dependent CV curves for MoNiFe/NF.

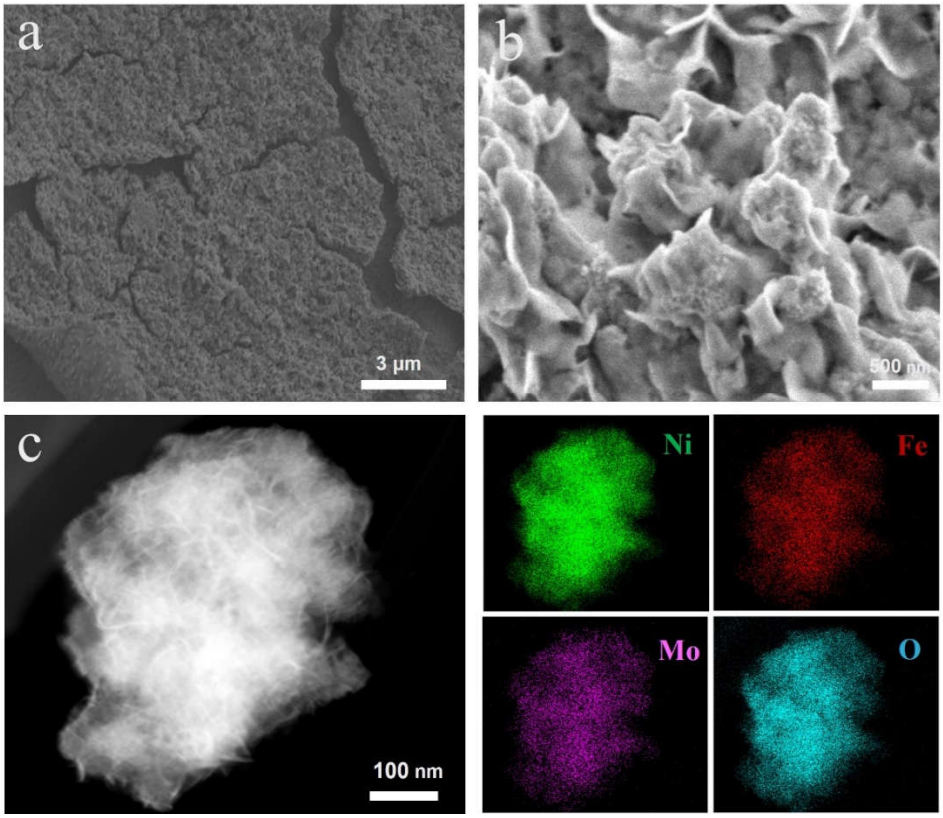

Fig. S8 SEM and TEM elemental mapping images of MoNiFe/NF after OER stability test for 170 h with different magnifications. (a, b) SEM; (c)TEM.

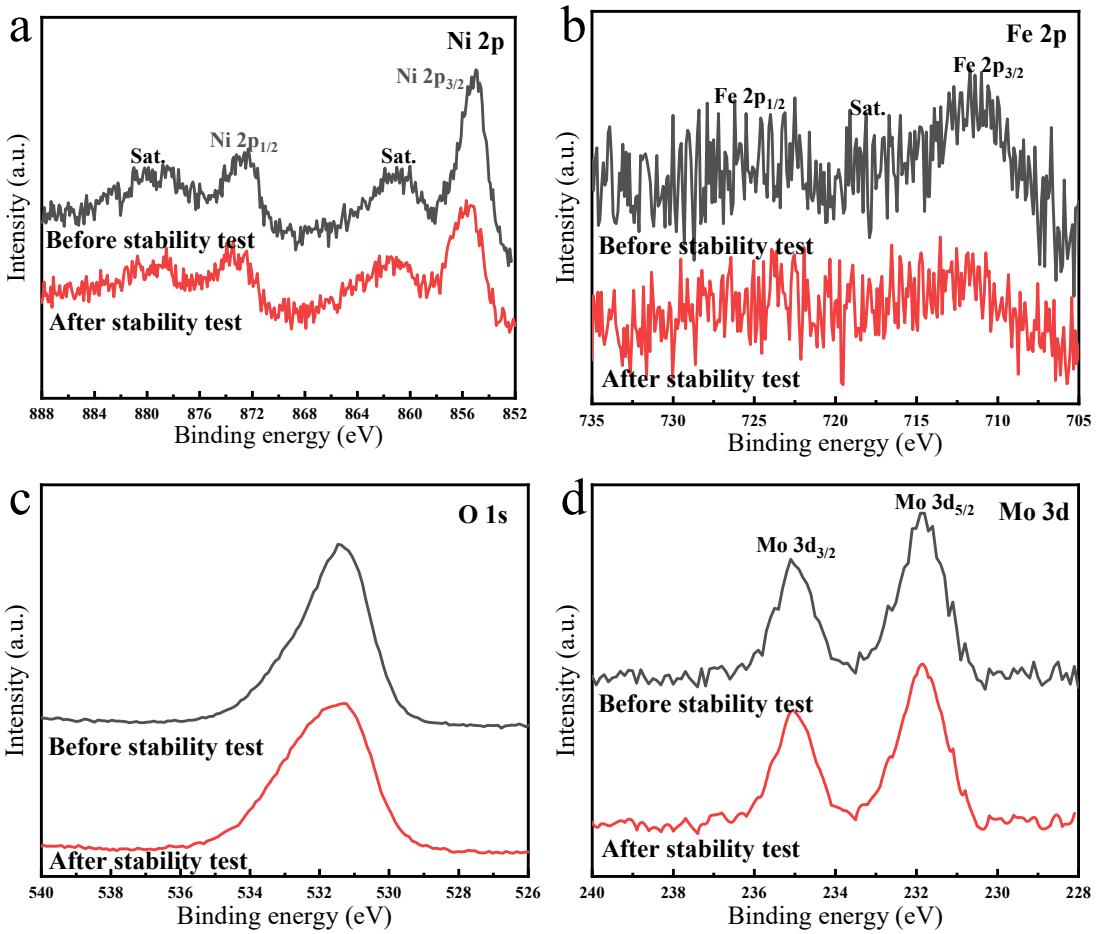

Fig. S9 XPS spectra comparison of fresh MoNiFe/NF and after OER stability tests.
(a) Ni 2p; (b) Fe 2p; (c) O 1s; (d) Mo 3d.

Fig. S10 Physical image of Faradic efficiency (FE) testing device.

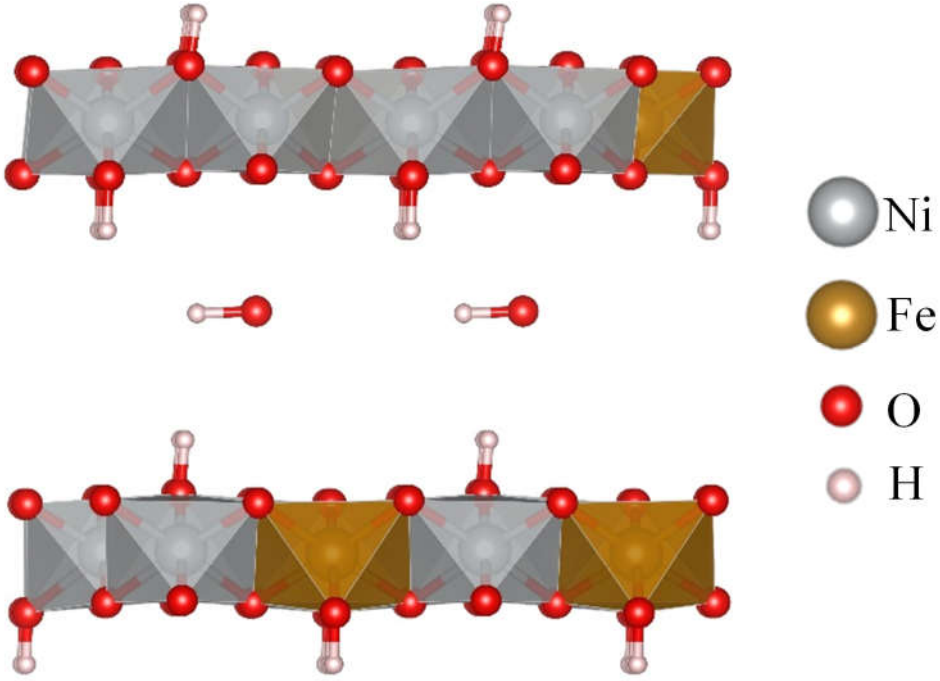

Fig. S11 Slab model for DFT calculations and slab model of NiFe/NF.

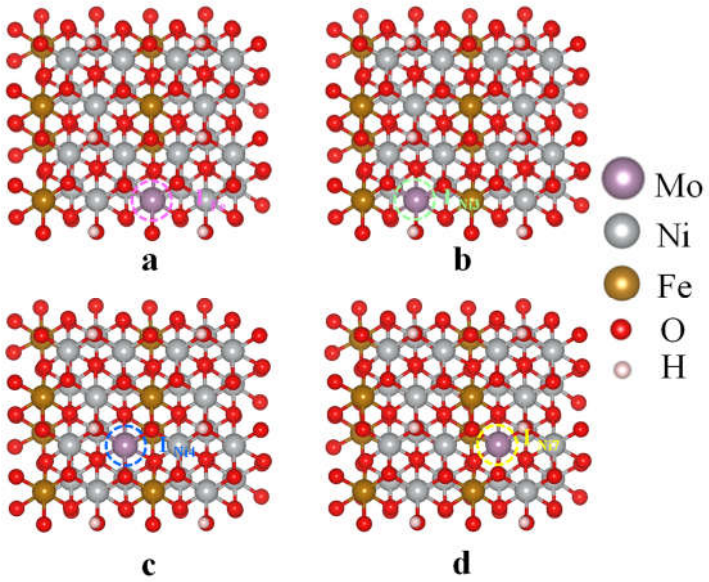

Fig. S12 Doping NiFe/NF with Mo at different sites.
(a) Surface Fe atom; (b) surface Ni3 atom; (c) surface Ni4 atom; (d) surface Ni7 atom replaced by Mo atom.

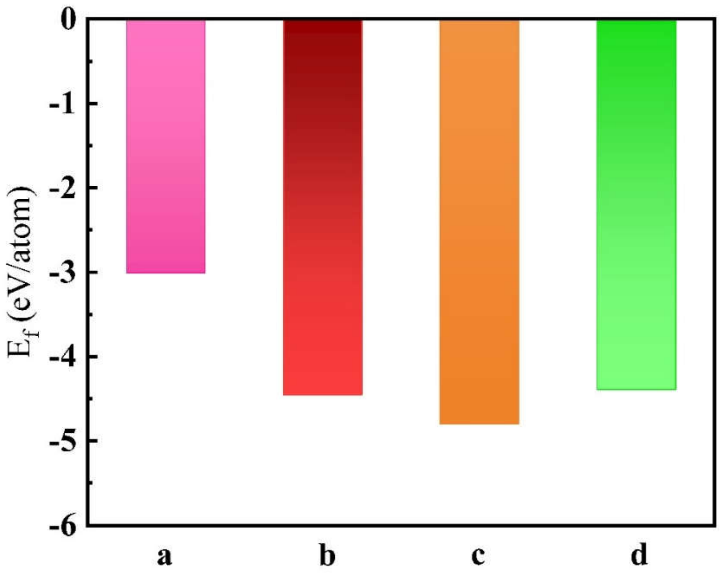

Fig. S13 Comparison of ΔE_f of configuration in Fig. S11 (a–d).

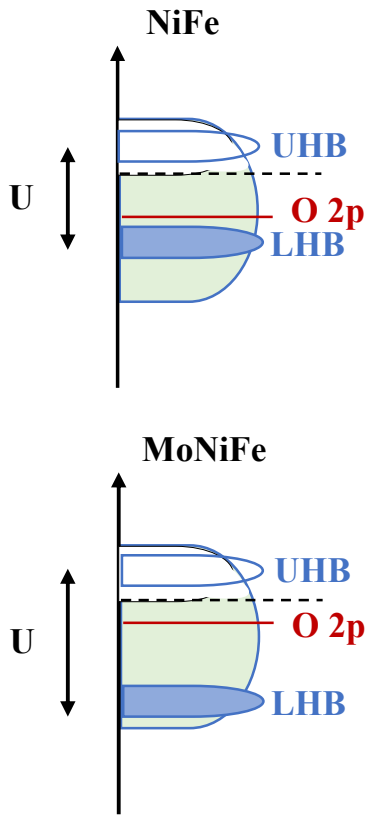

Fig. S14 Schematic band diagrams of NiFe/NF and MoNiFe/NF.

The *d*-orbitals split into electron-filled LHB and empty UHB with an energy difference of U. The LHB/UHB center is determined by the total metal 3*d*-orbital distribution below/above E_{Fermi} in DOS diagrams. Mo doping into NiFe/NF shifts the O 2p band towards the Fermi level. This shift decreases the distance between the O 2p band center and the Fermi level, facilitating electron flow away from oxygen sites under anodic potential, making lattice oxygen release easier.

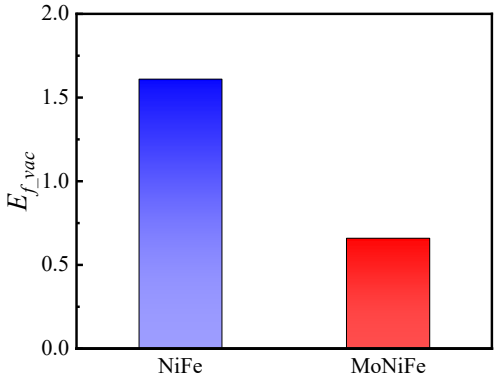

Fig. S15 Oxygen vacancy formation energy(E_{f_vac}) of NiFe/NF and MoNiFe/NF(To further confirm such impact of Mo doping, the oxygen vacancy formation energy (E_{f_vac}) was directly calculated. The E_{f_vac} of MoNiFe/NF was determined to be 0.66 eV, which was much lower than the 1.61 eV for the NiFe/NF.)

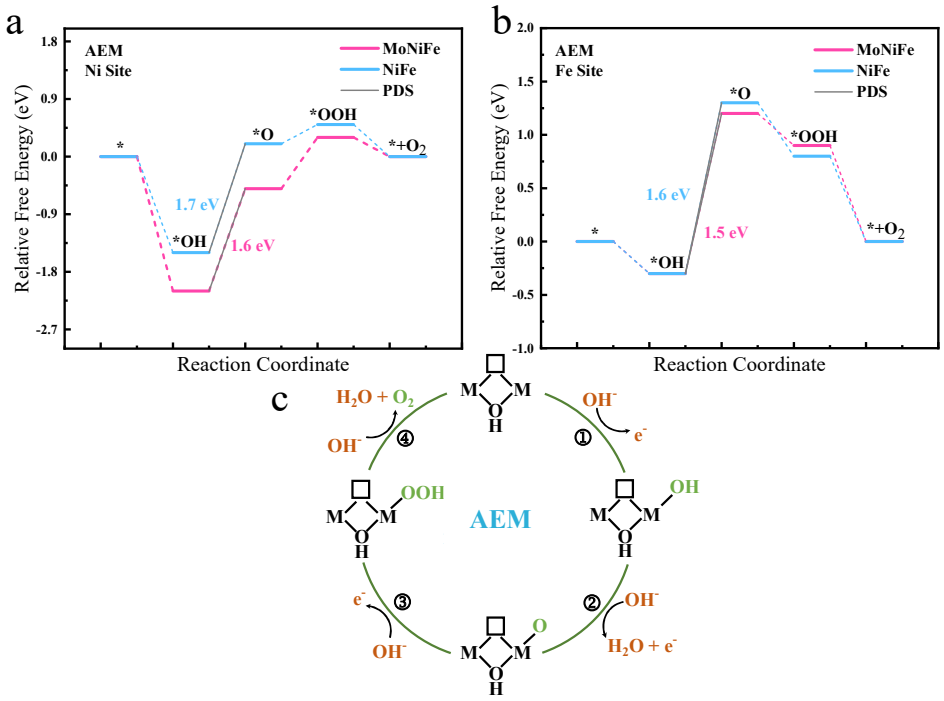

Fig. S16 Gibbs free energy diagrams of OER in AEM pathway.
(a) On Ni site; (b) on Fe site in NiFeOOH and MoNiFeOOH; (c) schematic illustration of AEM pathway.

The results show that deprotonation of *OH has the highest energy barriers for NiFe/NF and MoNiFe/NF, particularly at the RDS with an energy barriers of 1.7 and 1.6 eV on Ni and Fe sites, respectively. In contrast, deprotonation of *OH has an energy barrier of 1.6 and 1.5 eV on Ni and Fe sites for MoNiFe/NF, respectively.

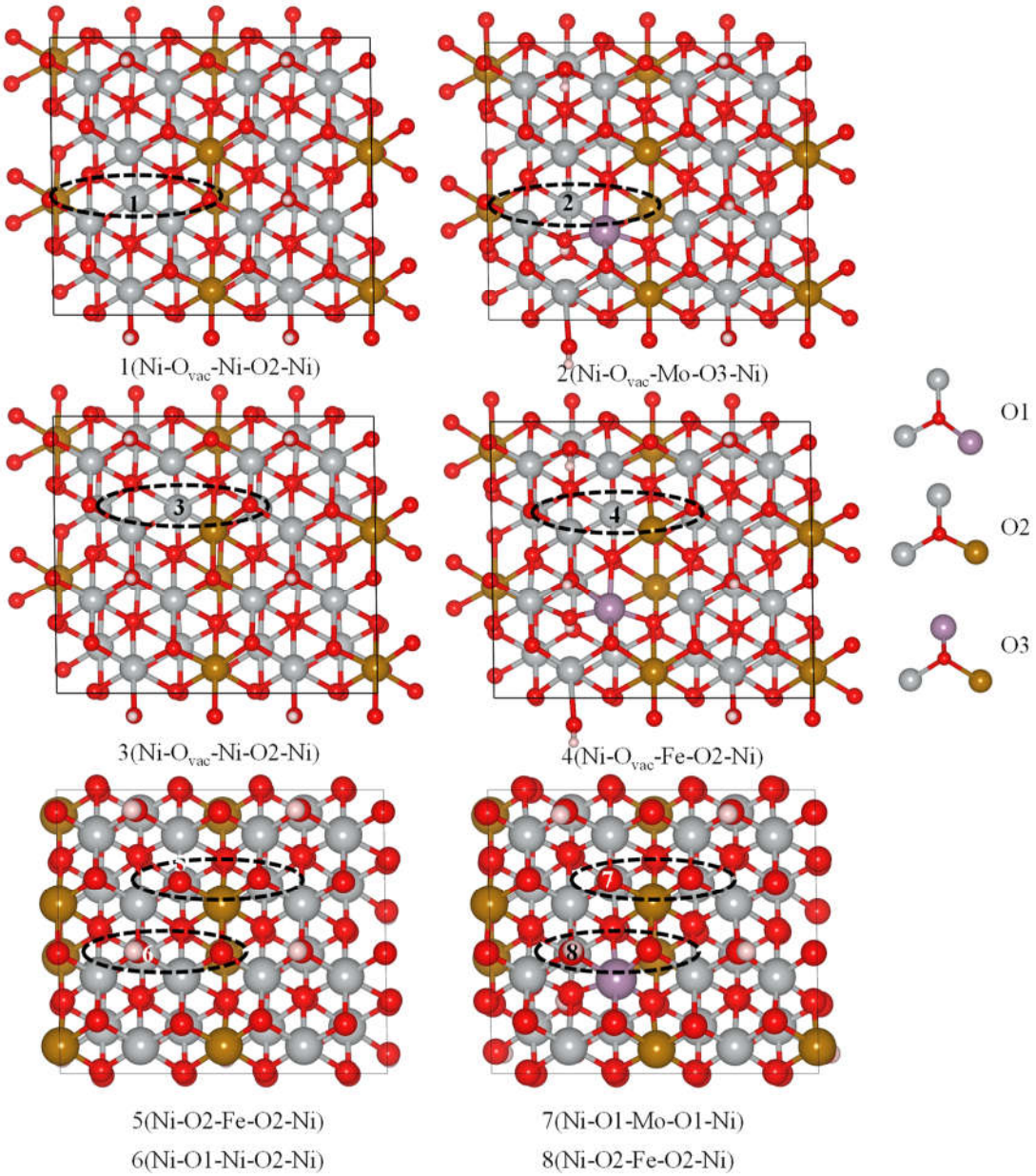

Fig. S17 Local configurations in NiFe/NF and MoNiFe/NF slab.

OER energetics was systematically correlated in the AEM and LOM pathways with different local configurations (i.e., Ni-O2-Fe-O2-Ni and Ni-O1-Ni-O2-Ni for NiFe/NF, Ni-O1-Mo-O1-Ni and Ni-O2-Fe-O2-Ni for MoNiFe/NF, as shown in Fig. S17).

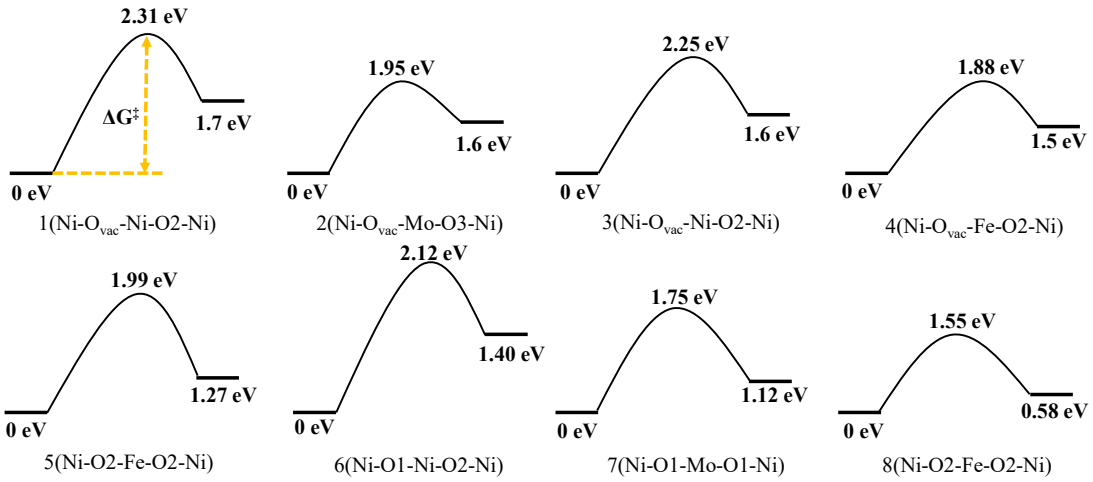

Fig. S18 Activation free energy ($\Delta G^{\ddagger}$) for NiFe/NF (1, 3, 5, 6) and MoNiFe/NF (2, 4, 7, 8) on different local configurations.

As seen above, the activation free energy ($\Delta G^{\ddagger}$) between the three isomeric intermediates of AEM M-OH→M-O (A1), LOM M-OH→M-O (L1), and LOM M-O→M-OOH (L2) are key to correlating the OER mechanism with different local configurations. For NiFe/NF, the $\Delta G^{\ddagger}$ for the formation of A1 is very high, with a barrier of 2.31 and 2.25 eV for Ni site and Fe site, respectively. For MoNiFe/NF, corresponding to Ni-Ovac-Mo-O3-Ni, Ni-Ovac-Fe-O2-Ni, Ni-O1-Mo-O1-Ni, and Ni-O2-Fe-O2-Ni, the OER still follows the LOM pathway. On Ni-Ovac-Mo-O3-Ni and Ni-Ovac-Fe-O2-Ni, the ΔG‡ for the formation of A1 is 1.95 and 1.88 eV, respectively, which is higher than that on Ni-O1-Mo-O1-Ni and Ni-O2-Fe-O2-Ni (1.55 and 1.75 eV) as shown in Fig. S18 and Table S6.

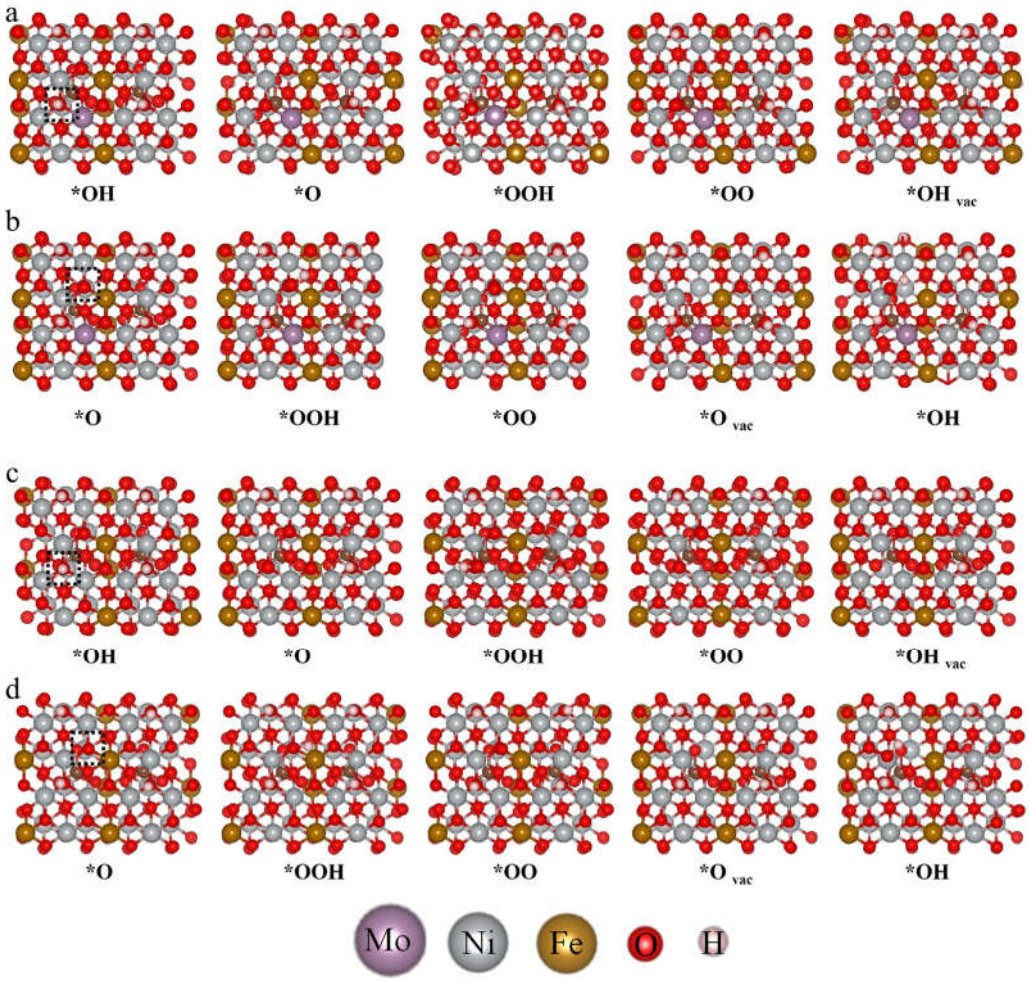

Fig. S19 Configurations for LOM pathway calculations.
(a, b) Configurations of MoNiFe/NF in LOM-1 and LOM-2 mechanisms; (c, d) configurations of NiFe/NF in LOM-1 and LOM-2 mechanisms.

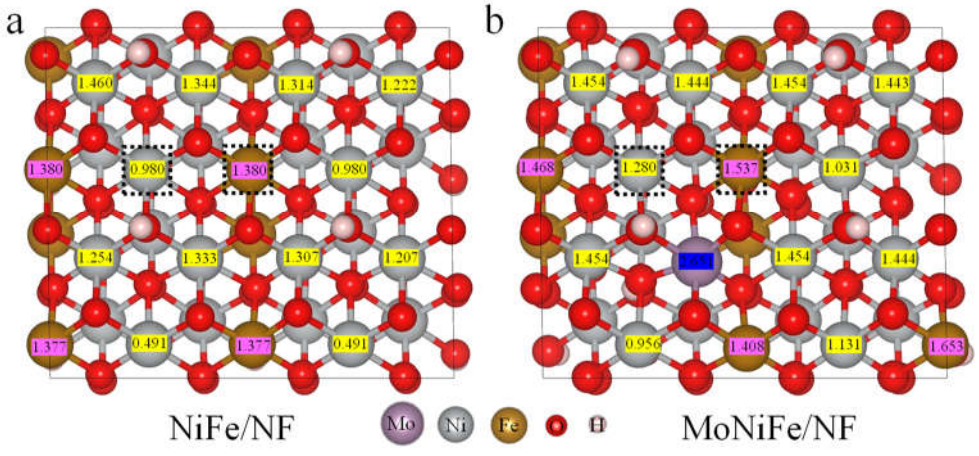

Fig. S20 Bader charge analysis.
(a) NiFe/NF; (b) MoNiFe/NF.

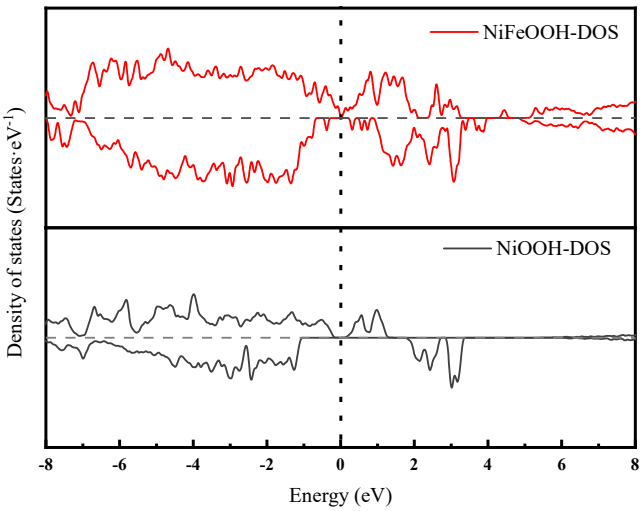

Fig. S21 DOS of Ni/NF and NiFe/NF.

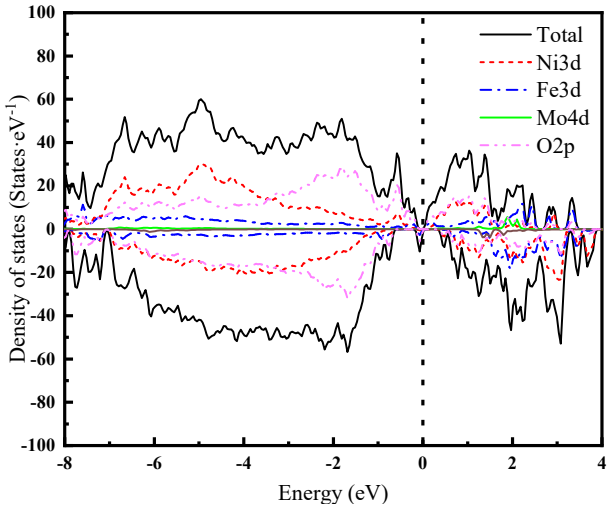

Fig. S22 DOS of MoNiFe/NF and NiFe/NF.

Table S1 Thermal corrections to Gibbs free energies of different adsorbates

	Pressure/bar	Temperature/K	*E*(DFT)/eV	Δ*G*/eV	*G*/eV
O_2(g)	1	298.15	-	-	−9.92
H_2(g)	1	298.15	−6.76	−0.045	−6.8
H_2O(l)	0.035	298.15	−14.22	−0.001	−14.22

Table S2 Thermal corrections to Gibbs free energies of different adsorbates

Adsorbate	G/eV[a]	$\Delta G_{0-298.15\,K}$[a]	ZPE/eV[a]	TS/eV[a]	ZPE/eV[b]	TS/eV[b]
*OO	-	0.07~0.09	0.13~0.15	0.21	0.17[b]	0.00[b]
*OH	-	0.36~0.38	0.38~0.39	0.05~0.06	0.30[b]	0.00[b]
*O	-	0.06~0.09	0.08~0.09	0.03~0.04	0.07[b]	0.00[b]
*OOH	-	0.40~0.43	0.46~0.48	0.12~0.14	0.44[c]	0.00[c]

a: This work. b: Data cited from Ref. [9]. c: Data cited from Ref. [10].

Table S3 ICP-MS results for MoNiFeOOH electrode

Samples	Element	Weight concentration /(mg·L^{-1})	Molecular concentration /(mmol·L^{-1})	Molecular ratio /%
MoNiFe/NF	Ni	16.74	0.29	57.54
	Fe	10.298	0.18	35.71
	Mo	3.3	0.034	6.75

Table S4 Comparison of OER activity of NiFeMo (in red) and recently reported benchmark catalysts

Catalysts	Support	Electrolyte	J/(mA·cm^{-2})	Overpotential/ mV	Tafel/ (mV·dec^{-1})	Ref.
MoNiFe	NF	1.0 M KOH	10	205	31.7	This work
NiFe	NF	1.0 M KOH	10	250	51.7	This work
NiFeCe−LDH/CNT	GC	1.0 M KOH	10	227	33	Xu et al. [11]
O−NiCoFe−LDH	CFP	0.1 M KOH	10	300	93	Qian et al. [12]
Au/NiFe−LDH	Iron foam	1.0 M KOH	10	210	40.4	Zhang [13]
NiFeV−LDHs/NF	NF	1.0 M KOH	10	231	39.4	Dinh et al. [14]
Cu@NiFe LDH	Cu foam	1.0 M KOH	10	199	27.8	Yu et al. [15]
NiFeCr−LDH	CFP	1.0 M KOH	25	225	69	Yang et al. [16]
Mn−doped NiFe−LDH	NF	1.0 M KOH	20	289	47	Lu et al. [17]

NiFeMn−LDH	CFP	1.0 M KOH	100	230	68.6	Zhou et al. [18]
CoFe LDHs−Ar	Ni Foam	1.0 M KOH	10	266	37.85	Wang et al. [19]
$Ni_3FeAl_{0.91}$−LDH@NF	NF	1.0 M KOH	20	304	57	Liu et al. [20]
NiFe−LDH film	GC	0.1 M KOH	20	250	40	Louie et al. [21]
NiFe−LDH/CNT	NF	1.0 M KOH	20	310	31	Gong et al. [22]
Amorphous NiFeMo	NF	1.0 M KOH	10	255	35	Li et al. [23]
Ce−NiFe LDH	NF	1.0 M KOH	10	205	37.9	Liu et al. [24]
Ni3Fe0.5V0.5	CFP	1.0 M KOH	100	264	39	Jiang et al. [25]
NiFeV−LDH	NF	1.0 M KOH	20	195	42	Li et al. [26]
NiFeCr	NF	1.0 M KOH	Onset	240	36	Bo et al. [27]

Table S5 LHB, UHB, and U for Ni and Fe sites on NiFeOOH and MoNiFeOOH

Slab models	site	LHB/eV	UHB/eV	*U*/eV
NiFeOOH	Ni	−4.41	2.13	6.54
	Fe	−3.97	2.21	6.18
MoNiFeOOH	Ni	−4.50	2.30	6.80
	Fe	−4.91	2.24	7.15

The specific positions of LHB and UHB were calculated to be −4.41, −3.97, and 2.13, 2.21 eV for Ni and Fe sites on NiFe/NF, and −4.50, −4.91, and 2.30, 2.24 eV for Ni and Fe sites on MoNiFe/NF, respectively. The *U* values of Ni and Fe sites on NiFe/NF and MoNiFe/NF were calculated to be 6.54, 6.80, and 6.18, 7.15 eV, respectively, indicating a stronger d-d Coulomb interaction after Mo doping. Such an enlarged *U* value gives rise to the downshift of LHB. (Fig. S14 and Table S5). It is noted that the LHB center is located beneath the O 2p band center. Therefore, the downshift of the LHB center and upshift of the O 2p band center for MoNiFe/NF lead to a smaller

overlap of metal 3d-orbital and oxygen 2p-orbital, which results in the weaker metal-oxygen bond. The weakened metal-oxygen bond, the upshifted O 2p band relative to Fermi level, and the enlarged U value in the MoNiFe/NF in comparison with the NiFe/NF indicate that Mo doping effectively activates the lattice oxygen, thereby promoting the oxygen vacancy formation process.

Table S6 Comparison of different local configurations to proceed OER by analysis

Local configurations	Slab models	OER mechanism	$\Delta G^{\ddagger}$/eV	ΔG/eV
Ni-Ovac-Ni-O2-Ni	NiFeOOH	AEM	2.31	1.70
Ni-Ovac-Mo-O3-Ni	MoNiFeOOH	AEM	1.95	1.60
Ni-Ovac-Ni-O2-Ni	NiFeOOH	AEM	2.25	1.60
Ni-O_{vac}-Fe-O2-Ni	MoNiFeOOH	AEM	1.88	1.5
Ni-O2-Fe-O2-Ni	NiFeOOH	LOM-2	1.99	1.27
Ni-O1-Ni-O2-Ni	NiFeOOH	LOM-1	2.12	1.4
Ni-O1-Mo-O1-Ni	MoNiFeOOH	LOM-2	1.75	1.12
Ni-O2-Fe-O2-Ni	MoNiFeOOH	LOM-1	1.55	0.58

Table S7 Calculated (PBE+U+D3) Gibbs free energies of OER on O and OH reactive sites of MoNiFe/NF and NiFe/NF structures

	Reaction Step (Formula)	Reactive Site	G/eV	ΔG/eV	Overpotential /eV
MoNiFe/NF	*OH + H_2O + 1/2H_2	OH	−601.48	0.44	1.12
	*O + H_2O + H_2		−596.40	1.12	
	*OOH + 3/2 H_2		−604.88	0.56	
	*OO + 2 H_2		−599.69	0.15	
	* + H_2O		−589.63	−2.26	
	*O + H_2O + H_2	O	−600.05	−0.41	0.58
	*OOH + 3/2 H_2		−610.05	0.22	
	*OO + 2 H_2		−605.20	−0.01	
	* + 2 H_2O		−595.29	−0.38	

	*OH + H_2O + 1/2 H_2		−605.26	0.58	
NiFe/NF	*OH + H_2O + 1/2 H_2	OH	−591.69	1.27	1.27
	*O + H_2O + H_2		−585.79	0.72	
	*OOH + 3/2 H_2		−594.66	−0.4	
	* + O_2 + 2 H_2		−590.43	0.30	
	* + 2 H_2O		−580.21	−1.89	
	*O + H_2O + H_2	O	−592.32	1.4	1.40
	*OOH + 3/2 H_2		−600.50	−0.16	
	* + O_2 + 2 H_2		−596.04	0.17	
	* + 2 H_2O		−585.95	−0.83	
	*OH + H_2O + 1/2 H_2		−596.37	−0.57	

References

[1] G. Kresse, J. Hafner, Ab initio molecular-dynamics simulation of the liquid-metal--amorphous-semiconductor transition in germanium, Phys. Rev. B: Condens. Matter, 49 (1994) 14251-14269

[2] G. Kresse, J. Hafner, Ab initio molecular dynamics for open-shell transition metals, Phys. Rev. B: Condens. Matter, 48 (1993) 13115-13118

[3] G. Kresse, J. Furthmüller, Efficient iterative schemes for ab initio total-energy calculations using a plane-wave basis set, Phys. Rev. B: Condens. Matter, 54 (1996) 11169-11186

[4] J.P. Perdew, K. Burke, M. Ernzerhof, Generalized gradient approximation made simple, Phys. Rev. Lett., 77 (1996) 3865-3868

[5] G. Kresse, D. Joubert, From ultrasoft pseudopotentials to the projector augmented-wave method, Phys. Rev. B: Condens. Matter, 59 (1999) 1758-1775

[6] P.E. Blöchl, Projector augmented-wave method, Phys. Rev. B: Condens. Matter, 50 (1994) 17953-17979

[7] J. Zhao, P. Zhang, T. Yuan, D. Cheng, S. Zhen, H. Gao, T. Wang, Z.-J. Zhao, J. Gong, Modulation of *CH_xO adsorption to facilitate electrocatalytic reduction of CO_2 to CH_4 over Cu-based catalysts, J. Am. Chem. Soc, 145 (2023) 6622-6627

[8] Z. Yan, H. Sun, X. Chen, H. Liu, Y. Zhao, H. Li, W. Xie, F. Cheng, J. Chen, Anion insertion enhanced electrodeposition of robust metal hydroxide/oxide electrodes for oxygen evolution, Nat. Commun., 9 (2018) 2373

[9] J.K. Nørskov, J. Rossmeisl, A. Logadottir, L. Lindqvist, J.R. Kitchin, T. Bligaard, H. Jónsson, Origin of the overpotential for oxygen reduction at a fuel-cell cathode, J. Phys. Chem. B, 108 (2004) 17886-17892

[10] M. Bajdich, M. García-Mota, A. Vojvodic, J.K. Nørskov, A.T. Bell, Theoretical investigation of the activity of cobalt oxides for the electrochemical oxidation of water, J. Am. Chem. Soc, 135 (2013) 13521-13530

[11] H. Xu, B. Wang, C. Shan, P. Xi, W. Liu, Y. Tang, Ce-doped NiFe-layered double hydroxide ultrathin nanosheets/nanocarbon hierarchical nanocomposite as an efficient oxygen evolution catalyst, ACS Appl. Mater. Interfaces, 10 (2018) 6336-6345

[12] L. Qian, Z. Lu, T. Xu, X. Wu, Y. Tian, Y. Li, Z. Huo, X. Sun, X. Duan, trinary layered double hydroxides as high-performance bifunctional materials for oxygen electrocatalysis, Adv. Energy Mater., 5 (2015) 1500245.

[13] J. Zhang, J. Liu, L. Xi, Y. Yu, N. Chen, S. Sun, W. Wang, K.M. Lange, B. Zhang, Single-atom Au/NiFe layered double hydroxide electrocatalyst: Probing the origin of activity for oxygen evolution reaction, J. Am. Chem. Soc, 140 (2018) 3876-3879.

[14] K.N. Dinh, P. Zheng, Z. Dai, Y. Zhang, R. Dangol, Y. Zheng, B. Li, Y. Zong, Q. Yan, Ultrathin porous NiFeV

ternary layer hydroxide nanosheets as a highly efficient bifunctional electrocatalyst for overall water splitting, Small, 14 (2018) 1703257.

[15] L. Yu, H. Zhou, J. Sun, F. Qin, F. Yu, J. Bao, Y. Yu, S. Chen, Z. Ren, Cu nanowires shelled with NiFe layered double hydroxide nanosheets as bifunctional electrocatalysts for overall water splitting, Energy Environ. Sci., 10 (2017) 1820-1827.

[16] Y. Yang, L. Dang, M.J. Shearer, H. Sheng, W. Li, J. Chen, P. Xiao, Y. Zhang, R.J. Hamers, S. Jin, Highly active trimetallic NiFeCr layered double hydroxide electrocatalysts for oxygen evolution reaction, Adv. Energy Mater., 8 (2018) 1703189.

[17] Z. Lu, L. Qian, Y. Tian, Y. Li, X. Sun, X. Duan, Ternary NiFeMn layered double hydroxides as highly-efficient oxygen evolution catalysts, Chem. Commun., 52 (2016) 908-911.

[18] D. Zhou, Z. Cai, Y. Jia, X. Xiong, Q. Xie, S. Wang, Y. Zhang, W. Liu, H. Duan, X. Sun, Activating basal plane in NiFe layered double hydroxide by Mn^{2+} doping for efficient and durable oxygen evolution reaction, Nanoscale Horizons, 3 (2018) 532-537.

[19] Y. Wang, Y. Zhang, Z. Liu, C. Xie, S. Feng, D. Liu, M. Shao, S. Wang, Layered double hydroxide nanosheets with multiple vacancies obtained by dry exfoliation as highly efficient oxygen evolution electrocatalysts, Angew. Chem. Int. Ed., 56 (2017) 5867-5871.

[20] H. Liu, Y. Wang, X. Lu, Y. Hu, G. Zhu, R. Chen, L. Ma, H. Zhu, Z. Tie, J. Liu, Z. Jin, The effects of Al substitution and partial dissolution on ultrathin NiFeAl trinary layered double hydroxide nanosheets for oxygen evolution reaction in alkaline solution, Nano Energy, 35 (2017) 350-357.

[21] M.W. Louie, A.T. Bell, An investigation of thin-film Ni–Fe oxide catalysts for the electrochemical evolution of oxygen, J. Am. Chem. Soc, 135 (2013) 12329-12337.

[22] M. Gong, Y. Li, H. Wang, Y. Liang, J.Z. Wu, J. Zhou, J. Wang, T. Regier, F. Wei, H. Dai, An advanced Ni–Fe layered double hydroxide electrocatalyst for water oxidation, J. Am. Chem. Soc, 135 (2013) 8452-8455.

[23] Y.-K. Li, G. Zhang, W.-T. Lu, F.-F. Cao, Amorphous Ni–Fe–Mo suboxides coupled with Ni network as porous nanoplate array on nickel foam: A highly efficient and durable bifunctional electrode for overall water splitting, Adv. Sci., 7 (2020) 1902034.

[24] M. Liu, K.-A. Min, B. Han, L.Y.S. Lee, Interfacing or doping? Role of Ce in highly promoted water oxidation of NiFe-layered double hydroxide, Adv. Energy Mater., 11 (2021) 2101281.

[25] J. Jiang, F. Sun, S. Zhou, W. Hu, H. Zhang, J. Dong, Z. Jiang, J. Zhao, J. Li, W. Yan, M. Wang, Atomic-level insight into super-efficient electrocatalytic oxygen evolution on iron and vanadium co-doped nickel (oxy)hydroxide, Nat. Commun., 9 (2018) 2885.

[26] P. Li, X. Duan, Y. Kuang, Y. Li, G. Zhang, W. Liu, X. Sun, Tuning electronic structure of NiFe layered double hydroxides with vanadium doping toward high efficient electrocatalytic water oxidation, Adv. Energy Mater., 8 (2018) 1703341.

[27] X. Bo, R.K. Hocking, S. Zhou, Y. Li, X. Chen, J. Zhuang, Y. Du, C. Zhao, Capturing the active sites of multimetallic (oxy)hydroxides for the oxygen evolution reaction, Energy Environ. Sci., 13 (2020) 4225-4237.